An anomalous Hall effect in altermagnetic ruthenium dioxide

Zexin Feng,[1, *] Xiaorong Zhou,[1, *] Libor Šmejkal,[2, 3, *] Lei Wu,[4, 5] Zengwei Zhu,[4, 5] Huixin Guo,[1] Rafael González-Hernández,[6, 2] Xiaoning Wang,[1] Han Yan,[1] Peixin Qin,[1] Xin Zhang,[1] Haojiang Wu,[1] Hongyu Chen,[1] Ziang Meng,[1] Zhengcai Xia,[4, 5] Jairo Sinova,[2, 3] Tomas Jungwirth,[3, 7] and Zhiqi Liu[1, †]

[1]*School of Materials Science and Engineering,*
Beihang University, Beijing 100191, China

[2]*Institut für Physik, Johannes Gutenberg Universität Mainz, 55128 Mainz, Germany*

[3]*Institute of Physics, Czech Academy of Sciences,*
Cukrovarnická 10, 162 00, Praha 6, Czech Republic

[4]*Wuhan National High Magnetic Field Center,*
Huazhong University of Science and Technology, Wuhan 430074, China

[5]*School of Physics, Huazhong University of Science and Technology, Wuhan 430074, China*

[6]*Grupo de Investigacíon en Física Aplicada, Departamento de Física,*
Universidad del Norte, Barranquilla, Colombia

[7]*School of Physics and Astronomy, University of Nottingham,*
NG7 2RD, Nottingham, United Kingdom

Abstract

Anomalous Hall effect is a time-reversal symmetry breaking electronic response discovered in ferromagnets in the 19th century and continuing to play a key role in modern fields of physics and nanoelectronics. In contrast, the antiparallel magnetic order on common rutile crystals served as a classic example which kept compensated magnets for nearly a century outside the focus of the magneto-electronic research. Breaking with this traditional perception, the antiparallel magnetic order on the rutile crystal of RuO_2 has been predicted to generate anomalous Hall effect of comparable strength to ferromagnets. Here we report the experimental demonstration of the anomalous Hall effect in RuO_2. We show that the effect arising from the antiparallel magnetic order dominates over an ordinary Hall contribution, and a contribution due to a weak field-induced magnetization. Our results open a prospect of research of relativistic topological Berry phases and dissipationless quantum transport in crystals of abundant elements and with a compensated antiparallel magnetic ordering at ambient conditions.

Main

The traditional perception of antiferromagnets, in line with the term itself, is that their behavior is opposite to ferromagnets. The latter are typically metallic and show strong magneto-electronic responses when their magnetization is reversed by, e.g., reversing a weak external magnetic field. Prominent examples of these responses are the relativistic anomalous Hall effect (AHE) in ferromagnetic films[1], and the non-relativistic giant magnetoresistance in ferromagnetic multilayers[2]. In contrast, starting from the pioneering works of Néel and his contemporaries, the classic antiferrmagnetic representatives where insulating rutile crystals, like FeF_2, with a compensating antiparallel ordering of moments on neighboring magnetic atoms[3–5]. Apart from being insulators, a basic symmetry principle would seem to exclude the above magneto-electronic effects. Omitting the non-magnetic atoms in the rutile crystals for brevity, any lattice constructed by a periodic repetition of pairs of magnetic atoms with mutually compensated antiparallel moments has a symmetry combining real-space inversion ($\mathcal{P}$) with time-reversal ($\mathcal{T}$) transformations[6,7]. For the $\mathcal{PT}$-symmetry of the antiferromagnetic crystal, Kramers theorem dictates that energy bands are spin degenerate,

2

which excludes the magneto-electronic responses like the AHE or GMR[7]. The perceived spin degeneracy of energy bands not only disqualified antiferromagnets for decades from the practically oriented magneto-electronic research, but also from basic studies of spin-polarized magnetic topological phases and relativistic Berry phase physics[1,7].

Intense research of the AHE beyond ferromagnetism was initiated in metallic crystals with three or four magnetic sublattices[8–14]. In this case, however, the magnetic order is compensated and breaks the $\mathcal{PT}$-symmetry in the expense of a strong non-collinearity of the magnetic moment vectors, typically due to frustrated exchange interactions on the lattice[7].

The prediction of the AHE in a classic rutile crystal has been made in RuO_2[15], in which an antiparallel magnetic order was recently discovered[16,17]. The material is of interest in the magneto-electronic research[15,18–23] for its metallic conduction, unique among the rutiles, and the inferred Néel temperature exceeding 300 K[16,17].

The theoretically predicted large relativistic Berry-phase AHE in RuO_2 is linked[7,15] to a spin-splitting and $\mathcal{T}$-symmetry breaking in the band structure[15,24–27]. The spin splitting, whose strength is comparable to ferromagnets but whose sign alternates across the magnetically compensated Brillouin zone, and the $\mathcal{T}$-symmetry breaking in the band structure have a leading strong non-relativistic origin[15,24–27]. It has inspired a reclassification of collinear magnetic phases based on a non-relativistic spin-symmetry group formalism, and to the delimitation of a separate symmetry class, dubbed altermagnetism[26,27]. This emerging phase has a characteristic alternating spin polarization in both real-space crystal structure and momentum-space band structure[26,27]. Apart from the AHE, altermagnets have been predicted to allow for robust non-relativistic spin-polarized currents that can facilitate counterparts of the GMR and other key non-relativistic phenomena employed for reading and writing information in ferromagnetic memories[18,22,23]. The predictions of the spin-polarized currents have been recently supported by initial transport experiments in RuO_2[19–21].

In this paper we give the experimental evidence of the AHE in RuO_2, consistent with the original theory prediction of this prominent magneto-electronic phenomenon[15]. Our work experimentally opens the research front, envisaged in the theoretical proposal of the AHE in RuO_2[15], of the topological Berry phase and dissipationless quantum transport in compensated collinear magnets[7]. As already pointed in the theory work on the AHE[15], RuO_2 is a representative of a remarkable type of crystal structures. The broken $\mathcal{PT}$-symmetry in the real-space crystal structure of rutiles, enabling the altermagnetic spin splitting and

3

$\mathcal{T}$-symmetry breaking in the electronic band structure, and the resulting AHE or GMR magneto-electronic responses[7,15,18–29], lies in the crystal field from the anisotropic arrangement of the non-magnetic atoms[15,26,27]. The mechanism was thus referred to as crystal $\mathcal{PT}$-symmetry breaking[15]. As illustrated in Fig. 1a, instead of the real-space inversion, the two crystal sublattices with opposite magnetic moments are connected by a real-space rotation transformation when the non-magnetic atoms are brought into the picture. The real-space rotation connecting the opposite-spin sublattices is the defining symmetry that results in the magnetically compensated phase, while allowing for the alternating spin splitting and $\mathcal{T}$-symmetry breaking in the band structure[26,27].

Before presenting our results, we emphasize the important role in our work of additional equilibrium relativistic effects which arise from the antiparallel magnetic order on the rutile crystal[30,31], in parallel to the non-equilibrium relativistic AHE[7,15]. The first of these effects is the magneto-crystalline anisotropy, described by relativistic spin-orbit coupling terms in the thermodynamic potential which depend on the crystallographic orientation of the Néel vector, $\mathbf{L} = \mathbf{M}_1 - \mathbf{M}_2$, of the antiparallel magnetic order[30,31]. (Here $\mathbf{M}_1$ and $\mathbf{M}_2$ are the moments on the opposite magnetic sublattices.) In the absence of an external magnetic field, the magneto-crystalline anisotropy in RuO_2 tends to align the Néel vector along the c-axis ([001]) of the tetragonal rutile crystal[15–17]. Incidentally, this is the singular crystal direction of the Néel vector for which the relativistic AHE arising from the antiparallel magnetic order is excluded by symmetry[15].

On the other hand, it is well documented in rutiles, both in theory and experiment[30], that the Néel vector can be reoriented from the easy axis by applying a magnetic field in the orthogonal direction to the easy axis. This is facilitated by the Zeeman term in the equilibrium thermodynamic potential, that couples the external magnetic field with a net magnetization $\mathbf{M} = \mathbf{M}_1 + \mathbf{M}_2$, and additional relativistic Dzyaloshinskii-Moriya interaction (DMI) terms, that couple the Néel vector with the net magnetization[30,31]. (In tetragonal crystals like RuO_2, the leading DMI terms are proportional to $(l_x m_y + l_y m_x)$, $(\mathbf{l} \cdot \mathbf{m})^2$ and $(\mathbf{l} \cdot \mathbf{m})l_x l_y$, where $\mathbf{l} = \mathbf{L}/|\mathbf{L}|$ and $\mathbf{m} = \mathbf{M}/|\mathbf{M}|$.[30]) We use the technique to experimentally induce and evidence the reorientation of the Néel vector from the zero-field easy axis in our RuO_2 samples. The results of the accompanying Hall measurements are consistent with the theoretically predicted dominant AHE contribution from the symmetry breaking by the antiparallel magnetic order on the rutile crystal (L-AHE), linked to the charge Hall

transport by the relativistic spin-orbit coupling[15]. In contrast, we confirm the expected weak contributions from a Lorentz-force ordinary Hall effect (OHE) due to the applied out-of-plane magnetic field, and from a weak field-induced out-of-plane magnetization (M-AHE).

Experimental method

By considering the established vector magnetometry technique in rutiles[30], and the symmetry of the L-AHE[15], we perform measurements in RuO_2 films oriented in the (110), (001), and (100)-planes. In all three sample geometries, the external magnetic field is applied along the normal to the film plane, as schematically illustrated in Fig. 1b-d.

The earlier theoretical and experimental vector magnetometry studies in rutiles with the [001] easy axis of the Néel vector showed[30], that a magnetic field applied along the [110] direction induces a continuous rotation of the Néel vector towards the [110] field direction in the $(1\bar{1}0)$-plane by an angle α (Fig. 1b), given approximately by $\sin\alpha \sim H/H_c$. Here H is the applied field, the sense of the rotation is given by the sign of H, and H_c is the scale of the field corresponding to the Néel vector reorientation into the [110]-axis. H_c depends on the exchange, magneto-crystalline anisotropy, and DMI terms of the thermodynamic potential[30]. It was shown[30] that in rutiles, H_c can be weaker than the spin-flop reorientation field applied along the [001] easy axis. Note that this phenomenology contrasts with antiferromagnets lacking the DMI terms, in which case a field applied in the transverse direction to the easy axis does not reorient the Néel vector, but induces canting of the moments and, at large fields, eventually enforces their parallel alignment.

In the rutiles, apart from the magnetization along the applied [110]-field, the reorientation of the Néel vector within the $(1\bar{1}0)$-plane away from the [001] easy axis is accompanied by a generation of a [001]-component of the magnetization, i.e., a component along the Néel vector easy axis and transverse to the applied field[30] (see Fig. 1b). In our vector magnetometry measurements, the detection of this magnetization component thus serves as an experimental signature of the Néel vector reorientation from the [001] axis.

Symmetry analysis and *ab initio* theory predict[15] that the reorientation of the Néel vector within the $(1\bar{1}0)$-plane generates a strong L-AHE in the RuO_2 film oriented in the (110)-plane, and that opposite sense of the Néel vector rotation gives opposite sign of the L-AHE. This allows us to detect the L-AHE signal that is odd in the applied [110]-field, and vanishes

at zero field. In Fig. 1e we use the (zero-field) *ab initio* theory of RuO_2[15] to further highlight the principles of our detection method, by plotting the dependence of the [001]-component of the magnetization and the [110]-component of the Hall vector, corresponding to the L-AHE signal detected in the (110)-oriented sample, on the angle of the Néel vector in the $(1\bar{1}0)$-plane. (For more details on the *ab initio* calculations and the choice of experimentally relevant parameters see Ref. 15, Methods and Extended Data Fig. 1 in the Supplementary Information.) We also emphasize that the sign of the field-induced magnetization vector and of the Hall vector are determined by the sign of the applied [110]-field, while they are independent of the initial sign of the Néel vector ([001] or [00-1]) at zero field. Therefore, the contribution to the L-AHE from domains with opposite Néel vector orientations at zero field add up when the Néel vector is reoriented from the easy axis by the applied [110]-field.

The RuO_2 sample oriented in the (001)-plane and the external magnetic field applied along the [001] axis serve as a reference (Fig. 1c). This sample and field geometry does not break the symmetry between opposite signs of the Néel-vector reorientation angle from the [001] easy axis[30]. Therefore, even if the applied field caused a Néel-vector reorientation, it would not generate a non-zero average magnetization component transverse to the applied magnetic field[30]. Similarly, the geometry would not lead to an L-AHE signal that is odd in the applied field[15]. This geometry can thus serve as a measure of the expected weak contributions from the OHE and M-AHE.

For the (100)-oriented sample and field applied along the [100]-axis, the Néel vector is not reoriented towards the field direction which makes this experimental geometry distinct from the (110)-oriented sample and field applied along the [110]-axis[30]. An additional distinction is that there is no magnetization component in the direction transverse to the magnetic field for the (100)-oriented sample and the field along the [100]-axis[30] (Fig. 1d). This applies even if the Néel vector were reoriented from the [001] easy axis (within the (100)-plane in this experimental geometry)[30]. Since we do not detect a measurable L-AHE signal in this geometry, it is used to reconfirm that the OHE and M-AHE contributions are isotropic in RuO_2, i.e. are independent of the film orientation, and reconfirm the quantitative measure of the OHE and M-AHE contributions. It then allows us to extract the L-AHE contribution from the measured Hall signals in the (110)-oriented samples.

We prepared the (110), (001), and (100)-oriented epitaxial films of rutile RuO_2 by pulsed-laser deposition on non-magnetic rutile TiO_2 substrates, that are isostructural and closely

lattice-matched to RuO_2, independent of the orientation of the growth plane. The three film orientations were grown simultaneously and, therefore, under identical conditions, to avoid differences due to unintentional variations in growth parameters. In a separate growth batch, we also prepared control samples on MgO and $SrTiO_3$ substrates. Transmission electron microscopy and X-ray diffraction pattern of optimized 27-nm-thick (110) RuO_2/TiO_2 are shown in Figs. 1c,d. Further details on the preparation and characterization of our samples are presented in the Supplementary Information Methods and Extended Data Figs. 3-10. We note that RuO_2 films grown on these substrates were used in the recent study demonstrating the high-temperature antiparallel magnetic order on the RuO_2 crystal[17], and in the parallel research of the non-relativistic magneto-electronic phenomena in RuO_2[19–21].

Magnetization and magneto-transport measurements

In Figs. 2a-c we summarize basic magnetic and electrical-transport characteristics of the (110), (001) and (100)-oriented RuO_2/TiO_2 films. All samples show a zero remanent magnetization, consistent with the compensated antiparallel magnetic order and the [001] easy axis of the Néel vector. Also consistent with the expected magnetic ordering, the induced moment along the applied magnetic field is weak, reaching 0.2 μ_B per Ru at 50 T. The moments are similar in all three sample orientations, with a slightly weaker susceptibility along the [001] easy axis of the Néel vector. (In Extended Data Figs. 4 we illustrate the exchange bias effect of RuO_2 on ferromagnetic CoFe deposited on top of RuO_2.)

The temperature-dependent resistivity (Fig. 2b) confirms the metallic character of the RuO_2 films. It is practically identical in the three sample orientations, thanks to our consistent sample preparation method, and in agreement with earlier reports[32] on isotropic resistivities of bulk single crystals of RuO_2. The cusp in the temperature-dependent resistivity curve[32], highlighted by the singularity in the temperature derivative of the resistivity (inset of Fig. 2b), is consistent with the Néel temperature above 300 K observed in earlier measurements on bulk and thin-film RuO_2 samples[16,17]. The longitudinal magnetoresistance is again identical in the three sample orientations (Fig. 2c). Its weak quadratic field-dependence is consistent with an ordinary (Lorentz force) positive-magnetoresistance origin.

The measured odd in magnetic field Hall signals are shown in Figs. 2d-f. At low temperatures, the field-dependent Hall resistivity of the (001) and (100)-oriented samples is nearly

identical, while the Hall signal of the (110)-oriented film is significantly stronger over the entire range of applied magnetic fields. Moreover, it shows a clear non-linearity at high fields, which is absent in the other two film orientations. Since the (001) and (100)-oriented samples have (nearly) identical ordinary magnetoresistance, magnetic moment induced along the field, and Hall signal, and since L-AHE is excluded by symmetry in the (001)-oriented film, we can ascribe the Hall signals in these two sample orientations to the sum of the OHE and M-AHE contributions. The independence of the OHE and M-AHE contributions on the sample orientation is further confirmed by the Hall measurements at high temperatures approaching the Néel temperature, at which the Hall signals in all three film orientations merge. We then attribute the additional contribution which dominates the lower-temperature Hall signals in the (110)-oriented film over the entire field-range to the L-AHE. The observed large magnitude and the high-field non-linearity of the Hall signal in the (110)-oriented sample suggests a sizable Néel vector reorientation in the explored field-range. Simultaneously we recall our *ab initio* calculations in Fig. 1e showing that L-AHE sharply increases from zero when the Néel vector is reoriented from the [001] easy axis towards the out-of-plane [110] direction, and that a large L-AHE signal can be expected well before the Néel vector is fully aligned with the [110]-axis.

In Fig. 3a,b we confirm by the independent vector magnetometry measurements that the Néel vector is reoriented in the (110)-film from the [001] easy axis, and that the reorientation is confined to the ($1\bar{1}0$)-plane. The clearly detectable [001] magnetization component, which is transverse to the field applied along the [110]-axis, is shown in Fig. 3a. As expected, it vanishes at low fields. With increasing the field strength, its magnitude abruptly increases, and the field-dependence levels off at the highest experimentally available field of 9 T. Since by symmetry, and as confirmed by our *ab initio* calculations in Fig. 1e, the [001] magnetization component should again vanish when the Néel vector is fully aligned with the [110]-axis, we conclude that the Néel vector reorientation angle is sizable, but far from complete at 9 T. An additional confirmation of the expected phenomenology is shown in Figs. 3c,d. Consistent with the earlier work[30], we do not observe any transverse magnetization components in the (001) and (100)-oriented samples.

Figures 4a,b summarize our experimental demonstration of the L-AHE by subtracting the measured Hall signals in the (001) and (100)-oriented samples, respectively, from the Hall signal of the (110)-oriented film. Consistent with the theory prediction for the Berry-phase

AHE mechanism[15] (see also Extended Data Fig. 1), we observe L-AHE resistivities which are comparable to metallic ferromagnets or non-collinear antiferromagnets, where AHE also dominates the OHE[1,7].

To confirm that our results are not specific to the RuO_2 films grown on the TiO_2 substrate, we performed control experiments on (110)-oriented RuO_2/MgO and (100)-oriented RuO_2/SrTiO$_3$ samples. The measurements, summarized in Figs. 4c,d, show identical phenomenology, and are in good quantitative agreement with the measurements on the RuO_2/TiO$_2$ films (see also Extended Data Figs. 7-9).

Discussion

Because we do not observe signatures of a full Néel vector reorientation into the (001) hard plane in our RuO_2 films, we cannot quantitatively infer from experiment the parameters of the thermodynamic potential, and the corresponding dependence of the Néel vector reorientation angle on the applied magnetic field[30]. We can, however, make the following estimates. The scale of the critical field applied along the [001] easy axis, corresponding to the abrupt spin-flop reorientation, is given by $H_{AE} = \sqrt{H_A H_E}$, where H_A is the anisotropy and H_E the exchange field. In the mean-field approximation, and considering the Néel temperature inferred from the resistivity measurements in our RuO_2 films (Fig. 2b), we estimate that $H_E \approx 350$ T. Our *ab initio* calculations shown in Supplementary Information Extended Data Fig. 1 indicate that H_A can reach a ≈ 50 T scale due to the strong relativistic spin-orbit coupling in RuO_2, resulting in a spin-flop field exceeding 100 T. This is consistent with the experimentally observed order of magnitude weaker spin-flop field in rutile CoF_2, whose Néel temperature and corresponding H_E are about 10 times smaller than in RuO_2, and whose weaker spin-orbit coupling gives also an order of magnitude smaller H_A[30]. It also explains why we do not observe a spin-flop signature in our measured magnetization curves up to the maxim applied magnetic field of 50 T.

For the in-plane hard-axis field along the [110] axis, the continuous field-induced reorientation is given approximately by $\sin \alpha \sim H/H_c$, where the reorientation-field scale, $H_c = (H_{AE} - H_d^2)/H_d$, was experimentally inferred in CoF_2 to be about 3/4 of the easy-axis spin-flop field[30]. (Here H_d is the relativistic Dzyaloshinskii-Moriya interaction (DMI) field[30].) Assuming that the relativistic DMI field in RuO_2 is again an order of magnitude

larger than in CoF_2, than the ratio between the easy-axis spin-flop field and the hard-axis reorientation field scale can be expected to be comparable in the two rutiles. This puts the estimated [110] reorientation-field scale in RuO_2 above 50 T, consistent with a sizable but not complete reorientation in our measurements performed up to 50 T.

In analogy to the AHE in ferromagnets, the L-AHE can in principle originate from scattering-independent intrinsic and side-jump mechanisms, and from the extrinsic skew-scattering mechanism[1]. Regarding the skew scattering contribution, previous studies in ferromagnets have shown that it becomes significant only in samples with conductivities above 10^6 $\Omega^{-1}cm^{-1}$, which is much higher than the conductivity of our RuO_2 films. The side-jump was shown in ferromagnets to be only a small correction of the scattering independent contribution[33]. As a result, theoretical studies of the scattering independent contribution to the AHE conductivity in ferromagnets and antiferromagnets have focused on the intrinsic Berry curvature mechanism[1,7]. *Ab initio* calculations of the intrinsic Berry curvature AHE tend to give a semiquantitative prediction of the AHE conductivity, but often disagree quantitatively with the measured values. For example, theory overestimates or underestimates by up to a factor of 3 the measured AHE conductivity in Ni or Fe, respectively[1].

In our case, the measured L-AHE conductivity exceeds 1000 $\Omega^{-1}cm^{-1}$ at 50 T. The *ab initio* magnitudes near the Fermi level peak at a value above 300 $\Omega^{-1}cm^{-1}$[15], which gives a comparable level of a semi-quantitative agreement between theory and experiment as in the conventional ferromagnets. In our case, the strong magnetic field used in the experiment can be an additional source of the quantitative discrepancy between the measured magnitude of the anomalous Hall conductivity and the *ab initio* Hall transport calculations performed at zero magnetic field[15]. In Supplementary Information Extended Data Fig. 2 we compare the *ab initio* equilibrium band structure of RuO_2 at zero field and at 50 T. The strong magnetic field generates only a weak magnetization on the ~ 0.1 μ_B per unit cell scale, consistent with experiment. Moreover, the overall character of the spin-split $\mathcal{T}$-symmetry broken band structures is similar in the zero-field and 50 T cases, supporting the expectation that the L-AHE origin is not principally affected by the applied magnetic field. Quantitatively, however, the small field-induced shifts of bands around the band (anti)-crossings, where the subtle relativistic Berry curvature tends to have the largest contributions[15], can quantitatively modify the resulting anomalous Hall conductivity.

Finally, we comment on our *ab initio* calculations of the dependence of the anomalous

Hall conductivity in RuO_2 on the Hubbard correlation parameter U for the Néel vector along the [110] axis, shown in Supplementary Information Extended Data Fig. 1. Values of $U \approx 1.6 - 2$ eV correspond to the magnitude of the sublattice magnetic moment consistent with previous *ab initio* studies[15–17,24]. The anomalous Hall conductivity peaks at $U \approx 1.6$ eV and vanishes at small values of U due to the vanishing magnetic order. (For large values of U the anomalous Hall conductivity vanishes due to the opening of an insulating band gap.) Since decreasing U in the *ab initio* calculations mimics the effect of an increasing temperature on the magnetic order, the steeply decreasing theoretical Hall conductivity with decreasing U is consistent with the experimentally observed drop in L-AHE with increasing temperatures.

Conclusions

By combining vector magnetometry and magneto-transport measurements on epitaxial RuO_2 films of different crystallographic orientations, we have experimentally demonstrated the AHE arising from the compensated collinear magnetic order on a classic rutile crystal structure. Our experimental observation removes the, often limiting, requirements of a ferromagnetic moment or a complex non-collinear magnetic order for observing this prominent relativistic magneto-electronic effect. Simultaneously, RuO_2 is only one example of a broad family of materials with compensated antiparallel magnetic order, allowing for strong spin-splitting and $\mathcal{T}$-symmetry breaking in the band structure, and the accompanying rich spin physics and magneto-electronics[7,15,18–29,34–41]. Our work thus may inspire new directions in frontier research of magnetic topological insulators, axion insulators, or quantum AHE systems[7,42,43] in the abundant class of collinear compensated magnets, many of which have high ordering temperatures and are composed of common elements.

Author contributions

Z.F. & Xiaorong Z. performed sample growth, electrical, structural and magnetic measurements with assistance from L.W., Z.Z., H.G., X.W., H.Y., P.Q., Xin.Z., H.W., H.C., Z.M. & Z.X. Theoretical calculations and data analysis were performed by L.S., R.G.H., J.S. & T.J. The manuscript was written by Z.L., Z.F. Xiaorong Z., L.S., J.S. & T.J. All authors commented on manuscript. This project was conceived and led by Z.L.

Competing interests

The authors declare no competing financial interests.

Additional information

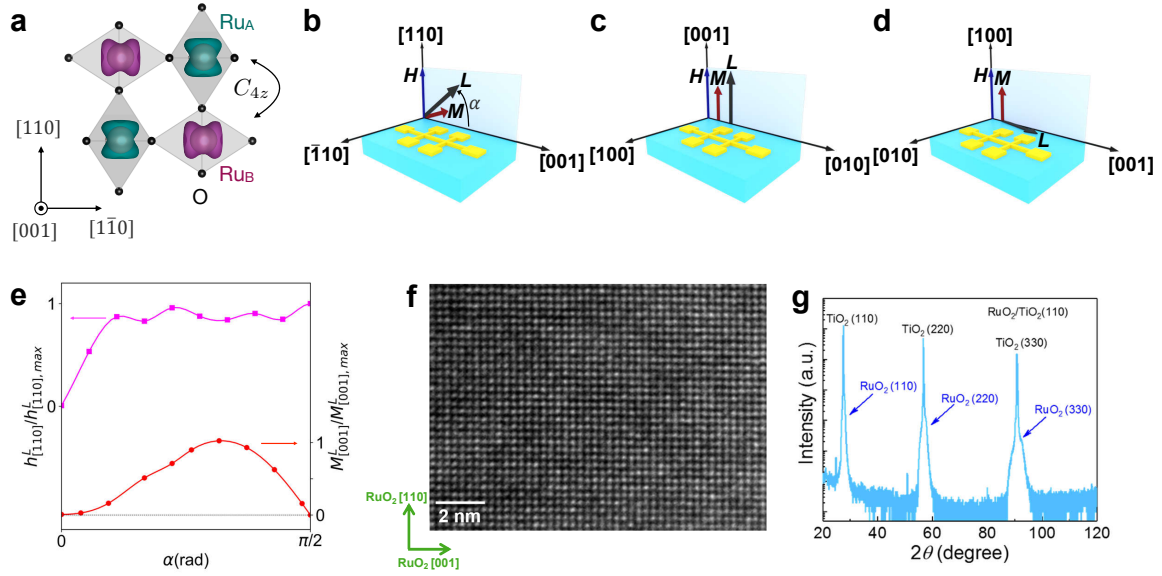Correspondence and requests for materials should be addressed to Z.L. (email: zhiqi@buaa.edu.cn).

Fig. 1. **Experimental method for detecting the anomalous Hall effect in RuO$_2$ a**, Schematic arrangement of Ru atoms with overlaid *ab intio* spin density iso-surfaces, and opposite-spin sublattices depicted by green and magenta colors. Schematic arrangement of O atoms is shown by black dots. Black double-arrow and its label highlight that the two crystal sublattices with opposite magnetic moments are connected by a real-space four-fold rotation transformation. **b-d**, Schematics of the three sample orientations used in the Hall measurements. Blue, brown and black arrows correspond to the applied magnetic field vector, magnetization vector and Néel vector, respectively. **e**, Zero-field *ab intio* calculation of a normalized [001]-component of the magnetization, $M_{[001]}^{\mathrm{L}}$, and a normalized [110]-component of the Hall vector, $h_{[110]}^{\mathrm{L}}$, corresponding to the Hall signal detected in the (110)-oriented sample, induced by the Néel vector rotated by an angle α from the [001]-axis in the (1$\bar{1}$0)-plane. **f**, Cross-section transmission electron microscopy image of an optimized (110)-oriented RuO$_2$/TiO$_2$ film. **g**, X-ray diffraction spectrum of the RuO$_2$/TiO$_2$ film, indicating a highly ordered (110) orientation of the RuO$_2$ film.
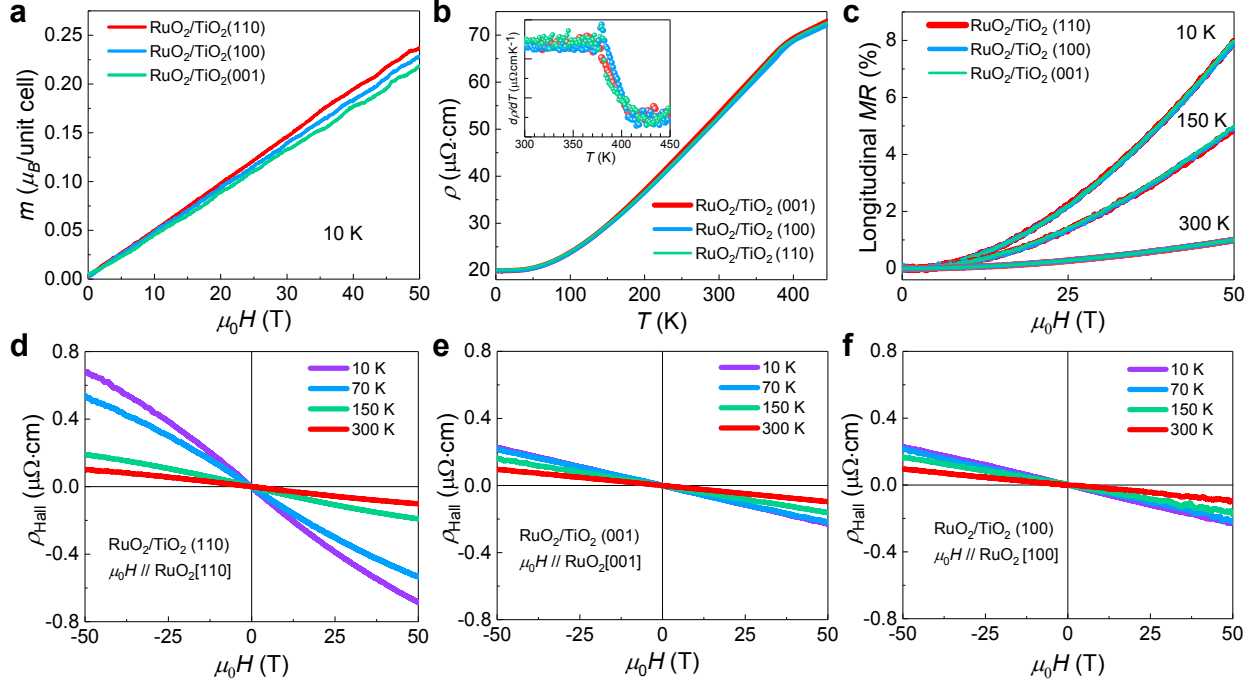
Fig. 2. **Magnetization and magneto-transport measurements a**, Magnetization along the applied out-of-plane magnetic field for the three RuO_2/TiO_2 film orientations. **b**, Resistivity versus temperature for the three film orientations. Inset: Temperature derivative of the resistivity highlighting the Néel temperature transport anomaly. **c**, Longitudinal magnetoresistance in the applied out-of-plane magnetic field at different temperatures. **d-f**, Hall signal at different temperatures for the three film orientations, respectively.
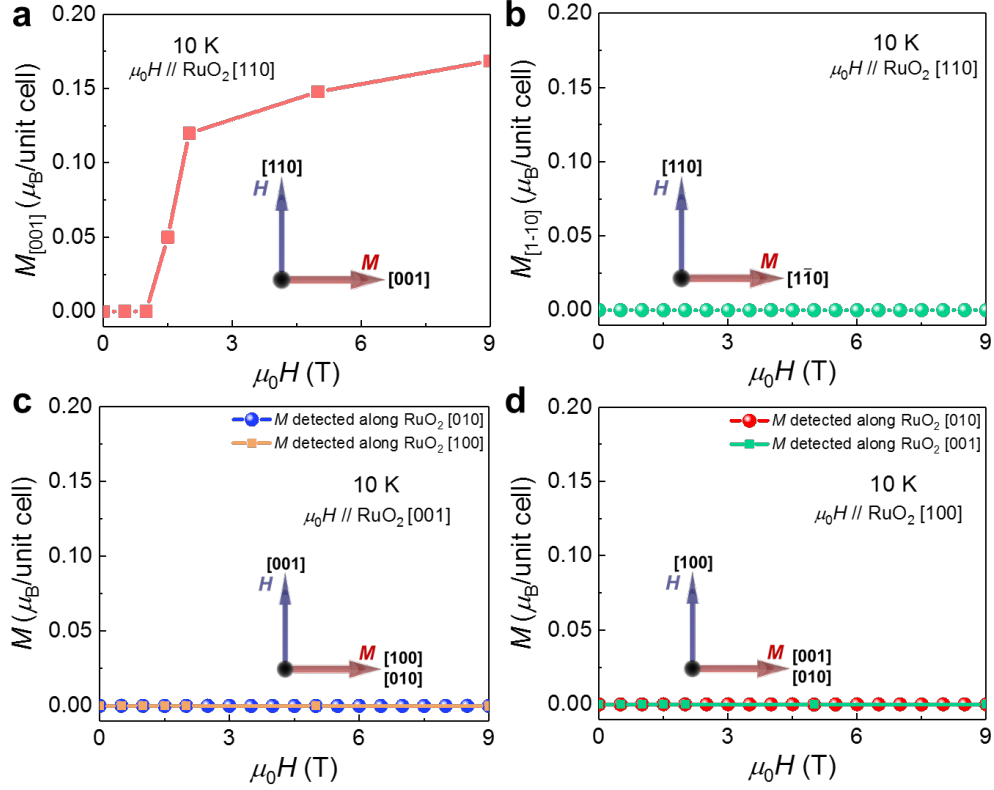
Fig. 3. **Measurememts of the magnetization components transverse to the applied magnetic field. a,b**, [001] and [1$\bar{1}$0] components, respectively, of the magnetization for the field applied along the [110]-axis in the (110)-oriented sample. **c**, [100] and [010] components of the magnetization for the field applied along the [001]-axis in the (001)-oriented sample. **d**, [001] and [010] components of the magnetization for the field applied along the [100]-axis in the (100)-oriented sample.
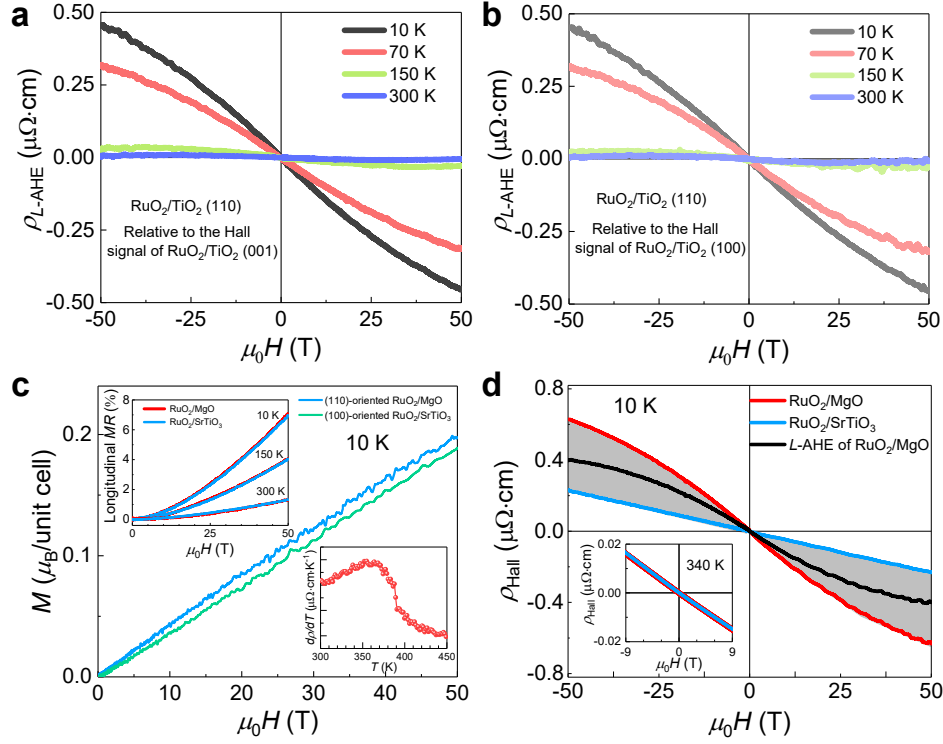
Fig. 4. **Anomalous Hall effect contribution (L-AHE) from the symmetry breaking by the antiparallel magnetic order on the rutile crystal. a,b**, L-AHE obtained by subtracting the measured Hall signals in the (001) and (100)-oriented samples, respectively, from the Hall signal of the (110)-oriented sample at different temperatures. **c**, Magnetization along the applied out-of-plane magnetic field in (110)-oriented RuO_2/MgO and (100)-oriented $RuO_2/SrTiO_3$ samples. Top inset: Longitudinal magnetoresistance in the applied out-of-plane magnetic field at different temperatures. Bottom inset: Temperature derivative of the resistivity highlighting the Néel temperature transport anomaly. **d**, Hall signals in the (110)-oriented RuO_2/MgO and (100)-oriented $RuO_2/SrTiO_3$ samples, and L-AHE obtained by subtracting the measured Hall signals in the (100)-oriented sample from the Hall signal of the (110)-oriented sample at 10 K. Inset: Hall signals of the two samples at 340 K.

* These authors contributed equally to this work.

† zhiqi@buaa.edu.cn

16

1 Nagaosa, N., Sinova, J., Onoda, S., MacDonald, A. H. & Ong, N. P. Anomalous Hall effect. *Reviews of Modern Physics* **82**, 1539–1592 (2010). URL https://link.aps.org/doi/10.1103/RevModPhys.82.1539. 0904.4154.

2 Chappert, C., Fert, A. & Van Dau, F. N. The emergence of spin electronics in data storage. *Nature Materials* **6**, 813–823 (2007). 1003.4058.

3 Néel, L. Some New Results on Antiferromagnetism and Ferromagnetism. *Reviews of Modern Physics* **25**, 58–63 (1953). URL http://physicstoday.scitation.org/doi/10.1063/1.3061199https://link.aps.org/doi/10.1103/RevModPhys.25.58.

4 Néel, L. Magnetism and Local Molecular Field. *Science* **174**, 985–992 (1971). URL http://www.sciencemag.org/cgi/doi/10.1126/science.174.4013.985http://www.ncbi.nlm.nih.gov/pubmed/17757022.

5 Kurti, N. *Selected Works of Louis Neel* (CRC Press, 1988), 1st edn.

6 Šmejkal, L., Železný, J., Sinova, J. & Jungwirth, T. Electric Control of Dirac Quasiparticles by Spin-Orbit Torque in an Antiferromagnet. *Physical Review Letters* **118**, 106402 (2017). URL https://link.aps.org/doi/10.1103/PhysRevLett.118.106402. 1610.08107.

7 Šmejkal, L., MacDonald, A. H., Sinova, J., Nakatsuji, S. & Jungwirth, T. Anomalous Hall antiferromagnets. *Nature Reviews Materials* published on–line 30 March (2022). URL http://arxiv.org/abs/2107.03321https://www.nature.com/articles/s41578-022-00430-3. 2107.03321.

8 Shindou, R. & Nagaosa, N. Orbital Ferromagnetism and Anomalous Hall Effect in Antiferromagnets on the Distorted fcc Lattice. *Physical Review Letters* **87**, 116801 (2001). URL https://link.aps.org/doi/10.1103/PhysRevLett.87.116801. 0108322.

9 Machida, Y., Nakatsuji, S., Onoda, S., Tayama, T. & Sakakibara, T. Time-reversal symmetry breaking and spontaneous Hall effect without magnetic dipole order. *Nature* **463**, 210–213 (2010).

10 Chen, H., Niu, Q. & Macdonald, A. H. Anomalous hall effect arising from noncollinear antiferromagnetism. *Physical Review Letters* **112**, 017205 (2014). 1309.4041.

11 Kübler, J. & Felser, C. Non-collinear antiferromagnets and the anomalous Hall effect. *Epl* **108**, 67001 (2014). 1410.5985.

12 Nakatsuji, S., Kiyohara, N. & Higo, T. Large anomalous Hall effect in a non-collinear antiferromagnet at room temperature. *Nature* **527**, 212–215 (2015). URL http://www.nature.com/

articles/nature15723;.

13. Kiyohara, N., Tomita, T. & Nakatsuji, S. Giant Anomalous Hall Effect in the Chiral Antiferromagnet Mn3Ge. *Physical Review Applied* **5**, 064009 (2016). 1511.04619.

14. Nayak, A. K. *et al.* Large anomalous Hall effect driven by a nonvanishing Berry curvature in the noncolinear antiferromagnet Mn3Ge. *Science Advances* **2**, e1501870–e1501870 (2016). 1511.03128.

15. Šmejkal, L., González-Hernández, R., Jungwirth, T. & Sinova, J. Crystal time-reversal symmetry breaking and spontaneous Hall effect in collinear antiferromagnets. *Science Advances* **6**, eaaz8809 (2020). URL `http://arxiv.org/abs/1901.00445https://advances.sciencemag.org/content/6/23/eaaz8809https://advances.sciencemag.org/content/6/23/eaaz8809.abstracthttps://advances.sciencemag.org/lookup/doi/10.1126/sciadv.aaz8809`. 1901.00445.

16. Berlijn, T. *et al.* Itinerant Antiferromagnetism in RuO2. *Physical Review Letters* **118**, 2–7 (2017). 1612.09589.

17. Zhu, Z. H. *et al.* Anomalous Antiferromagnetism in Metallic RuO2 Determined by Resonant X-ray Scattering. *Physical Review Letters* **122**, 017202 (2019). URL `http://arxiv.org/abs/1806.02036http://dx.doi.org/10.1103/PhysRevLett.122.017202https://link.aps.org/doi/10.1103/PhysRevLett.122.017202`. 1806.02036.

18. González-Hernández, R. *et al.* Efficient Electrical Spin Splitter Based on Nonrelativistic Collinear Antiferromagnetism. *Physical Review Letters* **126**, 127701 (2021). URL `http://arxiv.org/abs/2002.07073https://link.aps.org/doi/10.1103/PhysRevLett.126.127701`. 2002.07073.

19. Bose, A. *et al.* Tilted spin current generated by the collinear antiferromagnet RuO2 (2021). URL `http://arxiv.org/abs/2108.09150`. 2108.09150.

20. Bai, H. *et al.* Observation of spin splitting torque in a collinear antiferromagnet RuO2 (2021). URL `http://arxiv.org/abs/2109.05933`. 2109.05933.

21. Karube, S. *et al.* Observation of spin-splitter torque in collinear antiferromagnetic RuO_2 (2021). URL `http://arxiv.org/abs/2111.07487`. 2111.07487.

22. Šmejkal, L., Hellenes, A. B., González-Hernández, R., Sinova, J. & Jungwirth, T. Giant and Tunneling Magnetoresistance in Unconventional Collinear Antiferromagnets with Nonrelativistic Spin-Momentum Coupling. *Physical Review X* **12**, 011028 (2022). URL `http://arxiv.org/`

abs/2103.12664https://link.aps.org/doi/10.1103/PhysRevX.12.011028. 2103.12664.

23. Shao, D.-F., Zhang, S.-H., Li, M., Eom, C.-B. & Tsymbal, E. Y. Spin-neutral currents for spintronics. *Nature Communications* **12**, 7061 (2021). URL http://arxiv.org/abs/2103.09219https://www.nature.com/articles/s41467-021-26915-3. 2103.09219.

24. Ahn, K.-H., Hariki, A., Lee, K.-W. & Kuneš, J. Antiferromagnetism in RuO2 as d-wave Pomeranchuk instability. *Physical Review B* **99**, 184432 (2019). URL https://link.aps.org/doi/10.1103/PhysRevB.99.184432. 1902.04436.

25. Hayami, S., Yanagi, Y. & Kusunose, H. Momentum-Dependent Spin Splitting by Collinear Antiferromagnetic Ordering. *Journal of the Physical Society of Japan* **88**, 123702 (2019). URL https://journals.jps.jp/doi/10.7566/JPSJ.88.123702.

26. Šmejkal, L., Sinova, J. & Jungwirth, T. Altermagnetism: spin-momentum locked phase protected by non-relativistic symmetries (2021). URL http://arxiv.org/abs/2105.05820. 2105.05820.

27. Smejkal, L., Sinova, J. & Jungwirth, T. Emerging research landscape of altermagnetism (2022). 2204.10844.

28. Yuan, L.-D., Wang, Z., Luo, J.-W., Rashba, E. I. & Zunger, A. Giant momentum-dependent spin splitting in centrosymmetric low- ¡math¿ ¡mi¿Z¡/mi¿ ¡/math¿ antiferromagnets. *Physical Review B* **102**, 014422 (2020). URL https://arxiv.org/pdf/1912.12689.pdfhttps://link.aps.org/doi/10.1103/PhysRevB.102.014422.

29. Yuan, L.-D., Wang, Z., Luo, J.-W. & Zunger, A. Prediction of low-Z collinear and non-collinear antiferromagnetic compounds having momentum-dependent spin splitting even without spin-orbit coupling. *Physical Review Materials* **5**, 014409 (2021). URL https://journals.aps.org/prmaterials/pdf/10.1103/PhysRevMaterials.5.014409https://link.aps.org/doi/10.1103/PhysRevMaterials.5.014409.

30. Bazhan, A. N. & Bazan, C. Weak ferromagnetism in CoF2 and NiF2. *Sov Phys JETP* **42**, 898–904 (1976). URL http://www.jetp.ac.ru/cgi-bin/dn/e_042_05_0898.pdf.

31. Landau, L. & Lifshitz, E. *Electrodynamics of Continuous Media, vol. 8 of Course of Theoretical Physics* (Pergamon Press, Oxford, 1965), 2nd edn.

32. Ryden, W., Lawson, A. & Sartain, C. Temperature dependence of the resistivity of RuO2 and IrO2. *Physics Letters A* **26**, 209–210 (1968). URL https://linkinghub.elsevier.com/retrieve/pii/0375960168901266.

33 Weischenberg, J., Freimuth, F., Sinova, J., Blügel, S. & Mokrousov, Y. Ab Initio Theory of the Scattering-Independent Anomalous Hall Effect. *Physical Review Letters* **107**, 106601 (2011). URL `https://link.aps.org/doi/10.1103/PhysRevLett.107.106601`. 1108.5917.

34 Samanta, K. *et al.* Crystal Hall and crystal magneto-optical effect in thin films of SrRuO 3. *Journal of Applied Physics* **127**, 213904 (2020). URL `https://doi.org/10.1063/5.0005017http://aip.scitation.org/doi/10.1063/5.0005017`.

35 Hayami, S., Yanagi, Y. & Kusunose, H. Bottom-up design of spin-split and reshaped electronic band structures in antiferromagnets without spin-orbit coupling: Procedure on the basis of augmented multipoles. *Physical Review B* **102**, 144441 (2020). URL `https://journals.aps.org/prb/pdf/10.1103/PhysRevB.102.144441`.

36 Reichlova, H. *et al.* Macroscopic time reversal symmetry breaking arising from antiferromagnetic Zeeman effect. Tech. Rep. (2020). URL `https://arxiv.org/pdf/2012.15651.pdf`. 2012.15651v1.

37 Egorov, S. A. & Evarestov, R. A. Colossal Spin Splitting in the Monolayer of the Collinear Antiferromagnet MnF 2. *The Journal of Physical Chemistry Letters* **12**, 2363–2369 (2021). URL `https://pubs.acs.org/doi/10.1021/acs.jpclett.1c00282`.

38 Shao, D. F., Ding, J., Gurung, G., Zhang, S. H. & Tsymbal, E. Y. Interfacial Crystal Hall Effect Reversible by Ferroelectric Polarization. *Physical Review Applied* **15**, 1 (2021). URL `https://doi.org/10.1103/PhysRevApplied.15.024057`. 2006.09624.

39 Naka, M. *et al.* Spin current generation in organic antiferromagnets. *Nature Communications* **10**, 4305 (2019). URL `http://dx.doi.org/10.1038/s41467-019-12229-yhttp://www.nature.com/articles/s41467-019-12229-yhttps://doi.org/10.1038/s41467-019-12229-y`. 1902.02506.

40 Naka, M. *et al.* Anomalous Hall effect in ¡math¿ ¡mi¿κ¡/mi¿ ¡/math¿ -type organic antiferromagnets. *Physical Review B* **102**, 075112 (2020). URL `https://journals.aps.org/prb/pdf/10.1103/PhysRevB.102.075112https://link.aps.org/doi/10.1103/PhysRevB.102.075112`.

41 Mazin, I. I., Koepernik, K., Johannes, M. D., González-Hernández, R. & Šmejkal, L. Prediction of unconventional magnetism in doped FeSb2. *PNAS* **118**, e2108924118 (2021). URL `http://arxiv.org/abs/2105.06356`. 2105.06356.

42 Šmejkal, L., Mokrousov, Y., Yan, B. & MacDonald, A. H. Topological antiferromagnetic spintronics. *Nature Physics* **14**, 242–251 (2018). URL `http://arxiv.org/abs/1706.00670http:`

//www.nature.com/articles/s41567-018-0064-5. 1706.00670.

[43] Tokura, Y., Yasuda, K. & Tsukazaki, A. Magnetic topological insulators. *Nature Reviews Physics* **1**, 126–143 (2019). URL http://www.nature.com/articles/s42254-018-0011-5.